
BCONFORMER: A CONFORMER BASED ON MUTUAL SAMPLING FOR UNIFIED PREDICTION OF CONTINUOUS AND DISCONTINUOUS ANTIBODY BINDING SITES

Zhangyu You*, **Jiahao Ma***,
Material Innovation Institute for Life Sciences and Energy
The University of Hong Kong
Hetao SZ-HK Cooperation Zone
yzy48940@gmail.com, jiahao.ma@connect.hku.hk

Hongzong Li*,
Hong Kong Generative AI Research and Development Center
The Hong Kong University of Science and Technology
Hong Kong
lihongzong@ust.hk

Ye-Fan Hu*,[†]
Computational Immunology Centre
BayVax Biotech Limited
Hong Kong
yefan.hu@bayvaxbio.com

Jian-Dong Huang[†]
School of Biomedical Sciences
The University of Hong Kong
Hong Kong
jdhuang@hku.hk

ABSTRACT

Accurate prediction of antibody-binding sites (epitopes) on antigens is crucial for vaccine design, immunodiagnostics, therapeutic antibody development, antibody engineering, research into autoimmune and allergic diseases, and advancing our understanding of immune responses. Despite *in silico* methods that have been proposed to predict both linear (continuous) and conformational (discontinuous) epitopes, they consistently underperform in predicting conformational epitopes. In this work, we propose Conformer-based models trained separately on AlphaFold-predicted structures and experimentally determined structures, leveraging convolutional neural networks (CNNs) to extract local features and Transformers to capture long-range dependencies within antigen sequences. Ablation studies demonstrate that CNN enhances the prediction of linear epitopes, and the Transformer module improves the prediction of conformational epitopes. Experimental results show that our model outperforms existing baselines in terms of MCC, ROC-AUC, PR-AUC, and F1 scores on both linear and conformational epitopes. Code is available at <https://anonymous.4open.science/r/bconformer-epitope-519D>.

Keywords B-cell Epitope Prediction; Antigen–Antibody Interface; Conformer

1 Introduction

B cells are key effectors of the adaptive immune system, coordinating responses to pathogenic and aberrant signals. Each B cell expresses a single clonotype of B-cell receptor (BCR), a membrane-bound antibody that interacts with specific antigens. The binding sites on the antigen—known as the epitope—can be linear (continuous) or conformational

*Equal contribution.

[†]Corresponding authors.

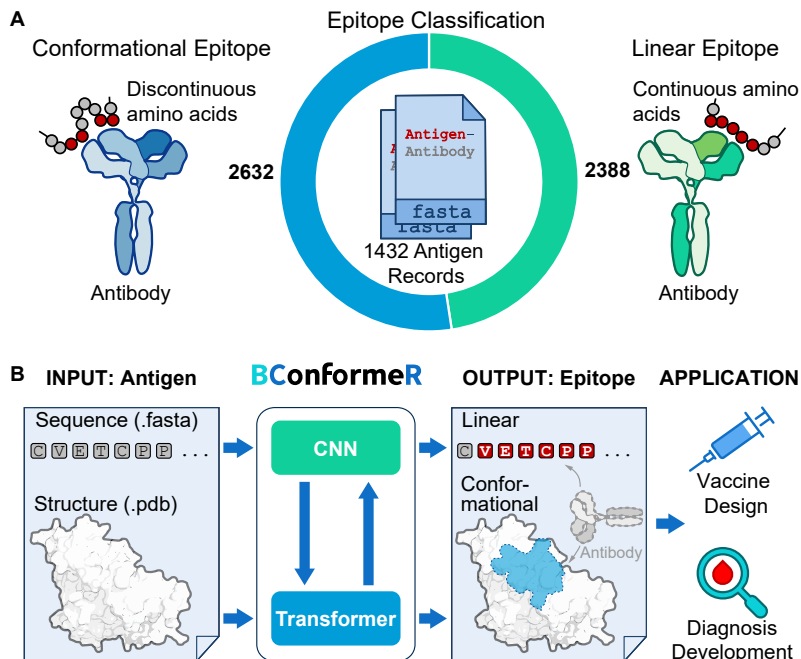


Figure 1: Overview of epitope classification and BConformerR prediction. (A) Epitopes, i.e., Antibody-binding sites, include conformational fragments ($n=2,632$) and linear regions ($n=2,388$). Data were derived from 1,432 antigen records. (B) Epitope prediction workflow. Antigen inputs are processed to predict linear and conformational epitopes, which enables applications in vaccine design and diagnostic development.

(discontinuous), and the corresponding binding sites on the antibody are called paratopes. Linear epitopes are formed by linear stretches of amino acid residues, while conformational epitopes are formed by distant residues brought together in 3D through folding.

Identifying epitopes is critical for antibody engineering [1, 2], disease diagnosis [3, 4], and vaccine optimization [5, 6]. Experimental techniques such as X-ray crystallography and cryo-electron microscopy provide high-resolution antigen-antibody (Ag-Ab) interactions but are resource-intensive [7, 8]. Phage display is faster but lacks atomic-level precision [9]. Therefore, many *in silico* methods have been developed to predict epitopes.

Sequence-based methods such as SEMA-1D [10, 11], BepiPred [12, 13, 14] and SEPPA [15] are widely used due to the availability of antigen sequences, with SEMA-1D 2.0 [11] and BepiPred-3.0 [14] notably improving performance by incorporating representations from the protein language model ESM-2 [16, 17]. Structure-based methods, such as SEMA-3D [10, 11], DiscoTope [18, 19], ScanNet [20] and Epitope3D [21], take the residue geometry and surface accessibility into consideration, but remain constrained by the limited availability of high-quality antigen structures. Among these methods, DiscoTope-3.0 [19] achieves the best performance in the benchmark evaluation.

However, epitope prediction remains a challenging task, with existing methods underperform on conformational ones. Moreover, there is a lack of hybrid backbone models to effectively handle both linear and conformational epitopes. A key source of this complexity stems from the nature of Ag-Ab interfaces, where linear epitopes are clustered along the sequence, and conformational epitopes are often spatially proximate but dispersed across different regions of the linear sequence [22]. To address this multi-scale complexity, we designed the Conformer architecture, which integrates convolution layers to learn local residue-level features and self-attention mechanisms to capture long-range dependencies within antigen sequences [23, 24].

Here, we propose **BConformer**, a **Conformer**-based model for continuous and discontinuous **BCR** epitope prediction. BConformer outperforms baselines—SEPPA-3.0, BepiPred-3.0, SEMA-1D 2.0 and DiscoTope-3.0—across multiple metrics, including MCC, ROC-AUC, PR-AUC, and F1 score on both linear and conformational epitopes. To further dissect the model’s design, we ablated ResNet bottlenecks and ViT modules from Conformer, showing that convolutional layers improve linear epitope prediction, and Transformer modules are critical for capturing discontinuous epitope patterns.

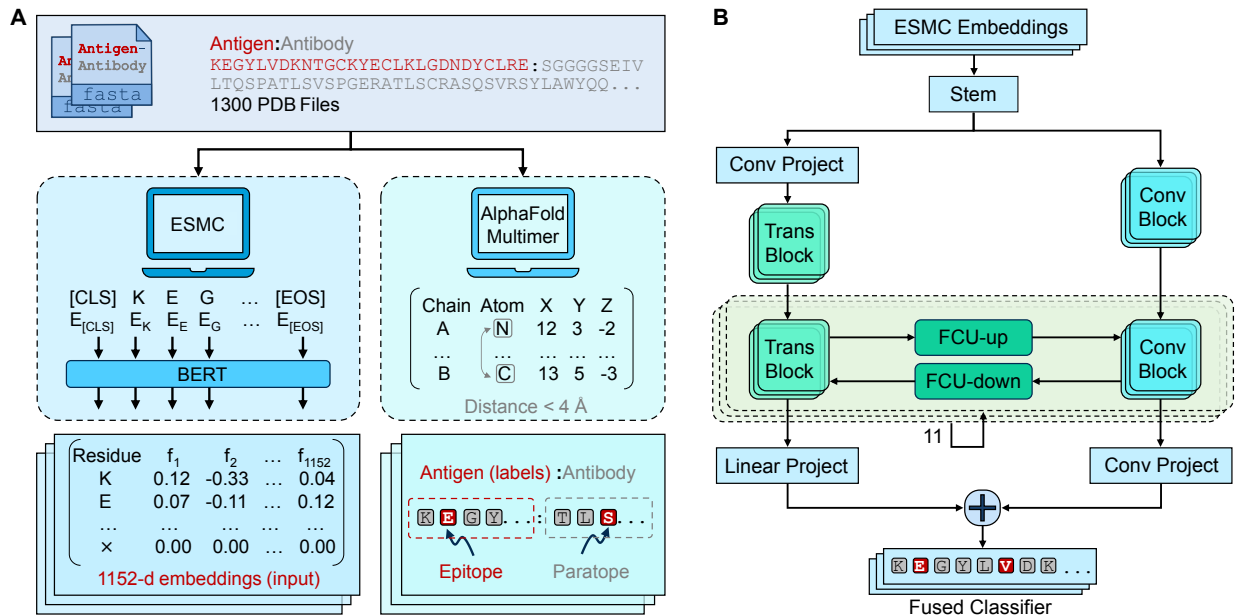


Figure 2: BConformerR overview. (A) Preparation pipeline. (Right) Preparation of AlphaFold-predicted structures and epitope extraction. (Left) Antigen embeddings. (B) Architecture overview. Stem module applies convolution and max-pooling to the ESM Cambrian (ESMC) embeddings; The Conv block and Trans block are based on ResNet bottleneck and Vision Transformer modules respectively; FCU-Up and FCU-Down connect the Conv and Trans blocks; The classifier linearly fuses features from both branches.

2 Methods

2.1 Epitope classification

To extract epitope residues, we define the residue–neighbor, where an antigen residue and an antibody residue are considered binding sites if the minimum distance between any pair of their heavy atoms is less than 4 Å [25]. Generally, epitopes are separated into multiple Regions (R) and Fragments (F) for each antigen sequence. Regions are defined as linear stretches of antigen sequence having at least three antibody-contacting residues. Gaps between contacting residues are allowed, and a gap size of up to three non-contacting residues is chosen on the basis of the structure of α -helices, which enables residues on the same helical face to be included [26]. Fragments, which do not contain enough antibody-contacting residues to qualify as a region, are considered discontinuous in our study (Fig. 1A).

For real and predicted annotations, linear and discontinuous epitopes are extracted from regions and fragments, respectively. Ambiguous cases occur when the real and predicted labels differ, especially when a residue is annotated as part of a region in the ground truth but as part of a fragment in the prediction, or vice versa. To address this, all classifications are determined based on the ground-truth labels. That is, for a real label $r \in \{N, L, D\}$ and predicted label $p \in \{N, L, D\}$, the final classification $c(r, p)$ is defined as:

$$c(r, p) = \begin{cases} L, & (r, p) \in \{(L, \cdot), (N, L)\} \\ D, & (r, p) \in \{(D, \cdot), (N, D)\} \\ N, & (r, p) = (N, N) \end{cases} \quad (1)$$

where N , L , and D denote non-epitope, linear epitope and discontinuous epitope, respectively. Performance metrics (e.g., F1) are then calculated for each type of epitopes.

2.2 Conformer

2.2.1 Overview

To take advantage of both local and global representations for epitope prediction, we construct BConformerR, a dual-branch architecture adapted from Conformer [24]. BConformerR consists of a shared convolutional stem, a CNN

	stage 1			stage 2			stage 3		
CNN	$\begin{bmatrix} 1, 144 \\ 3, 144 \\ 1, 576 \end{bmatrix}$	$\begin{bmatrix} 1, 144 \\ 3, 144 \\ 1, 576 \end{bmatrix}$	$\begin{bmatrix} 1, 144 \\ 3, 144 \\ 1, 576 \end{bmatrix}$	$\begin{bmatrix} 1, 288 \\ 3, 288 \\ 1, 1152 \end{bmatrix}$	$\begin{bmatrix} 1, 288 \\ 3, 288 \\ 1, 1152 \end{bmatrix}$	$\begin{bmatrix} 1, 576 \\ 3, 576 \\ 1, 2304 \end{bmatrix}$	$\begin{bmatrix} 1, 576 \\ 3, 576 \\ 1, 2304 \end{bmatrix}$	$\begin{bmatrix} 1, 576 \\ 3, 576 \\ 1, 2304 \end{bmatrix}$	
FCU	—	$\begin{matrix} [1, 1536] \\ \downarrow \end{matrix}$	$\begin{matrix} \uparrow \\ [1, 144] \end{matrix}$	$\begin{matrix} [1, 1536] \\ \downarrow \end{matrix}$	$\begin{matrix} \uparrow \\ [1, 288] \end{matrix}$	$\begin{matrix} [1, 1536] \\ \downarrow \end{matrix}$	$\begin{matrix} \uparrow \\ [1, 576] \end{matrix}$	$\begin{matrix} [1, 1536] \\ \downarrow \end{matrix}$	
Trans	$\begin{bmatrix} \text{MHSA-24, 1536} \\ 1, 3072 \\ 1, 1536 \end{bmatrix}$	$\begin{bmatrix} \text{MHSA-24, 1536} \\ 1, 3072 \\ 1, 1536 \end{bmatrix}$	$\begin{bmatrix} \text{MHSA-24, 1536} \\ 1, 3072 \\ 1, 1536 \end{bmatrix}$	$\begin{bmatrix} \text{MHSA-24, 1536} \\ 1, 3072 \\ 1, 1536 \end{bmatrix}$	$\begin{bmatrix} \text{MHSA-24, 1536} \\ 1, 3072 \\ 1, 1536 \end{bmatrix}$	$\begin{bmatrix} \text{MHSA-24, 1536} \\ 1, 3072 \\ 1, 1536 \end{bmatrix}$	$\begin{bmatrix} \text{MHSA-24, 1536} \\ 1, 3072 \\ 1, 1536 \end{bmatrix}$	$\begin{bmatrix} \text{MHSA-24, 1536} \\ 1, 3072 \\ 1, 1536 \end{bmatrix}$	
	$\times 1$	$\times 3$	$\times 3$	$\times 4$					

Table 1: Interaction layers of BConformer. MHSA denotes multi-head self-attention.

branch, a Transformer branch, Feature Coupling Units (FCUs) for bidirectional feature exchange, and two per-position classifiers (Fig. 2B).

Sequences are padded to match the longest length in each batch. The stem consists of a 1D convolution and a 1D max pooling, with the embedding dimension C (e.g., 1152 generated by ESMC-600M) reduced to $C/4$ channels after the stem. Then as shown in Table 1, both branches process initial features and no feature coupling is applied in the first block. From the second block onward, FCUs are inserted to progressively fuse local and global representations. At each stage, CNN-derived features are passed to the Transformer branch, and Transformer-derived global representations are fed back to the CNN branch. The CNN branch gradually expands to $2C$ channels, and the Transformer branch maintains D -dimensional (e.g., 1536) token embeddings at the end.

Finally, a 1D convolutional classifier and a linear classifier are applied to the outputs of the CNN and Transformer branches, respectively, producing per-residue logits $\mathbf{y}_{\text{CNN}}, \mathbf{y}_{\text{Trans}} \in \mathbb{R}^{L \times 2}$. These are linearly fused and converted to per-residue class probabilities using the softmax function:

$$\mathbf{p}_i = \text{softmax}(\alpha \mathbf{y}_{\text{CNN},i} + (1 - \alpha) \mathbf{y}_{\text{Trans},i}), \quad (2)$$

where $\mathbf{y}_i \in \mathbb{R}^2$ denotes the logits for the i -th residue, and α is the weighted parameter.

2.2.2 CNN branch

The CNN branch is composed of three stages after the stem, each consisting of repeated convolutional blocks based on the ResNet bottleneck design [27]. As shown in Table 1, given an input $\mathbf{x} \in \mathbb{R}^{C' \times L}$, the bottleneck performs three sequential convolutions with a residual connection applied to \mathbf{x} :

$$\begin{aligned} \mathbf{z}_1 &= \sigma(\text{BN}_1(\text{Conv}_{1 \times 1}(\mathbf{x}))), \\ \mathbf{z}_2 &= \sigma(\text{BN}_2(\text{Conv}_{3 \times 1}(\mathbf{z}_1))), \\ \mathbf{z}_3 &= \text{BN}_3(\text{Conv}_{1 \times 1}(\mathbf{z}_2)), \\ \mathbf{y} &= \sigma(\mathbf{z}_3 + \mathcal{F}(\mathbf{x})), \end{aligned} \quad (3)$$

where $\sigma(\cdot)$ denotes the ReLU activation, BN represents 1D batch normalization, and

$$\mathcal{F}(\mathbf{x}) = \begin{cases} \mathbf{x} & \text{if shape matches} \\ \text{BN}_{\text{res}}(\text{Conv}_{1 \times 1}(\mathbf{x})) & \text{otherwise} \end{cases}$$

The channel dimension is first downsampled, then expanded by a factor of 4 within each bottleneck. The first convolution block contains a single bottleneck, while subsequent blocks include bottlenecks before and after the Transformer branch.

2.2.3 Transformer branch

The Transformer branch processes embeddings using 12 repeated Transformer blocks, with each block following a structure similar to ViT [28]. As shown in Table 1, given the input $\mathbf{x} \in \mathbb{R}^{L \times D}$, a single Transformer block updates the representation as follows:

$$\begin{aligned} \mathbf{z}_1 &= \mathbf{x} + \text{DropPath}(\text{MHSA}(\text{LN}_1(\mathbf{x}))), \\ \mathbf{z}_2 &= \mathbf{z}_1 + \text{DropPath}(\text{MLP}(\text{LN}_2(\mathbf{z}_1))), \end{aligned} \quad (4)$$

where MHSA(\cdot) denotes the multi-head self-attention mechanism with h (e.g., 24) heads [29], and MLP(\cdot) consists of a linear up-projection to $2D$ dimensions, a GELU activation, followed by a linear down-projection to D . The DropPath operator implements stochastic depth regularization.

Since the CNN branch already encodes positional information, no explicit positional embeddings are added. Also, we omit the use of [CLS] tokens as our task is residue-level classification. This branch facilitates the modeling of long-range interactions between residues, preserving spatial information of discontinuous epitopes.

2.2.4 Feature coupling units

To enable bidirectional interaction between local CNN features and global Transformer representations, we introduce feature coupling units (FCUs) from the second block. FCU-Down projects CNN features into the Transformer space and adds them to the Transformer input:

$$\begin{aligned} \mathbf{F}_{\text{CNN}}^{\rightarrow} &= \left(\text{BN}(\text{Conv}_{1 \times 1}(\mathbf{F}_{\text{CNN}}))\right)^T, \\ \tilde{\mathbf{F}}_{\text{Trans}} &= \mathbf{F}_{\text{Trans}} + \mathbf{F}_{\text{CNN}}^{\rightarrow}. \end{aligned} \quad (5)$$

FCU-Up maps Transformer features back to the CNN space and merges them:

$$\begin{aligned} \mathbf{F}_{\text{Trans}}^{\leftarrow} &= \text{BN}(\text{Conv}_{1 \times 1}(\tilde{\mathbf{F}}_{\text{Trans}}^T)), \\ \tilde{\mathbf{F}}_{\text{CNN}} &= \mathbf{F}_{\text{CNN}} + \mathbf{F}_{\text{Trans}}^{\leftarrow}. \end{aligned} \quad (6)$$

2.3 Calibrated Score

Scores of residues in each antigen are normalized using the following formula:

$$z_i = \frac{s_i - \mu_{\text{antigen}}}{\sigma_{\text{antigen}}}, \quad (7)$$

where s_i denotes the raw score of residue i , and μ_{antigen} and σ_{antigen} represent the mean and standard deviation of scores for that antigen, respectively. Both μ_{antigen} and σ_{antigen} are estimated using two separate generalized additive models (GAMs) [30], with one predicting the mean residue score from antigen length and the other predicting the standard deviation from the mean residue score [19].

3 Experiments

3.1 Experiments Setup

3.1.1 Dataset

We trained two models separately using experimentally solved and AlphaFold-predicted structures. The dataset of experimentally solved Ag–Ab complexes was obtained from AACDB [31]. Redundant complexes were removed by retaining only one complex for each PDB ID, resulting in a curated dataset of 3,674 Ag–Ab complexes for training. For the AlphaFold-based dataset, we collected 1,300 Ag–Ab complex FASTA files from AbEpiTope-1.0 [32] and modeled each complex using AlphaFold-2.3 ColabFold [33]. Thirty structural predictions were generated for each complex, producing a total of 39,000 structures. For each complex, we retained the top-ranked model and discarded those with a pLDDT score below 0.82. After extracting epitopes for each complex, we further excluded those with insufficient epitope residues. The final dataset contained 1,180 Ag–Ab complexes, of which 1,080 were used for training BConformerR and 100 for validation and ablation studies.

As the datasets used among methods are not consistent, we assembled a SARS-CoV-2 test set from CoV-AbDab [34] for models trained on experimentally solved structures, and selected 24 antigen records from the SEMA-1D 2.0 test sets to construct a blind test set for AlphaFold-based models.

3.1.2 Calibrated score

After training, the μ_{antigen} and σ_{antigen} were estimated from the predicted score distributions (Fig. 3A,B). The scores were then calibrated based on different antigen lengths, which effectively reduced false positives while improving the true positive rate (Fig. 3C,D).

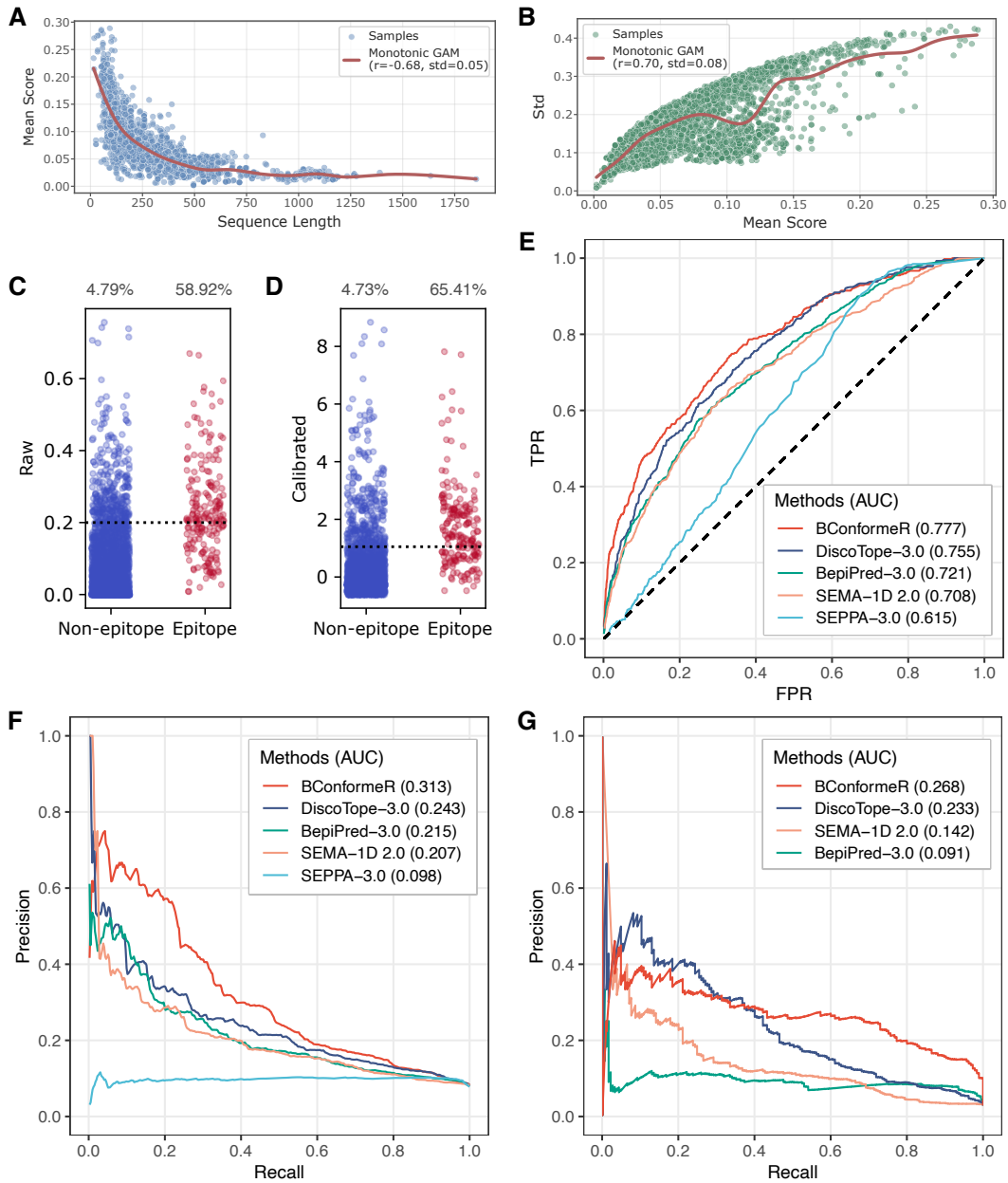


Figure 3: Improved performance of BConformerR. (A–B) GAMs for estimating μ and std. (C–D) Comparison between raw and calibrated scores on the SARS-CoV-2 test set. (E–F) ROC-AUC and PR-AUC; BConformerR trained on AlphaFold-predicted structures and evaluated on the blind test set of 24 antigens. (G) PR-AUC; BConformerR trained on experimentally solved structures and evaluated on the SARS-CoV-2 test set.

3.2 Comparison with SOTA Methods

3.2.1 Benchmark evaluation

BConformerR outperforms state-of-the-art baselines, achieving superior ROC-AUC and PR-AUC on AlphaFold-predicted structures (Fig. 3E,F) and higher PR-AUC on SARS-CoV-2 test set (Fig. 3G). Notably, it consistently improves the prediction of both linear and discontinuous epitopes (Tab. 2), demonstrating robust identification of epitope regions and fragments.

Method	Alphafold structures			Solved structures		
	F1-L \uparrow	F1-D \uparrow	MCC \uparrow	F1-L \uparrow	F1-D \uparrow	MCC \uparrow
SEPPA-3.0	0.158 \pm 0.009	0.237 \pm 0.025	0.058 \pm 0.014	-	-	-
BepiPred-3.0	0.276 \pm 0.007	0.209 \pm 0.011	0.194 \pm 0.003	0.299 \pm 0.009	0.087 \pm 0.001	0.153 \pm 0.005
SEMA-1D 2.0	0.270 \pm 0.005	0.213 \pm 0.006	0.188 \pm 0.002	0.327 \pm 0.008	0.106 \pm 0.007	0.193 \pm 0.004
DiscoTope-3.0	0.303 \pm 0.007	0.231 \pm 0.004	0.227 \pm 0.007	0.396 \pm 0.023	0.095 \pm 0.007	0.307 \pm 0.006
BConformerR	0.349 \pm 0.004	0.262 \pm 0.003	0.296 \pm 0.003	0.405 \pm 0.004	0.135 \pm 0.014	0.350 \pm 0.014

Table 2: Performance comparison of different methods. F1-L and F1-D refer to the F1 scores calculated on linear and discontinuous epitopes, respectively. Standard deviation calculated over a range of thresholds.

3.3 Ablation

3.3.1 Overview

To further assess the contribution of each module to linear and conformational epitope prediction, we ablated the dual-branch Conformer into standalone ResNet and ViT variants. We first reduced the depth of BConformer-12 (BConformerR) to evaluate the effectiveness of the original architecture. Then, ResNet1D-152 and ResNet1D-101, as well as ViT1D-12 and ViT1D-9, were selected based on comparable parameters (Params) and multiply-accumulate operations (MACs) to BConformer-9 and BConformer-6 respectively. The F1 score was used as the primary evaluation metric for both linear and discontinuous epitope prediction.

3.3.2 Conformer vs. CNN

Purely convolutional variants capture contiguous residue patterns efficiently and therefore achieve competitive scores on linear epitopes. However, their strictly local receptive field prevents them from modelling long-range residue couplings that dominate conformational epitopes. As shown in Table 3, ResNet1D-152 attains the highest linear F1 score (0.462) among all models, confirming its effectiveness on local patterns. However, its discontinuous F1 drops to 0.272, lower than BConformer-9 (0.309) and ViT1D-12 (0.298), pointing to difficulty in capturing discontinuous dependencies.

By injecting a Transformer branch and exchanging information through FCUs, BConformer-9 achieves a noticeably higher discontinuous F1 than ResNet1D-152, while keeping a linear F1 of 0.445 with only a minor drop. This shows that substituting part of the convolutional layers with a Transformer modules improves discontinuous epitope prediction with little sacrifice in linear performance.

3.3.3 Conformer vs. ViT

Vision Transformer variants excel at aggregating sequence-wide information but lack explicit inductive bias for short-range motifs, often resulting in underfitting on linear stretches and noisy attention over densely packed regions. As shown in Table 3, ViT1D-9 achieves a discontinuous F1 of 0.292, surpassing ResNet1D-101 (0.240), ResNet1D-152 (0.272) and BConformer-6 (0.270). However, this comes at the cost of reduced performance on linear epitopes, where ViT1D-9 (0.415) trails behind ResNet1D-101 (0.423) and BConformer-6 (0.419).

Model	Linear			Discontinuous			Params (M)	MACs (G)
	Prec \uparrow	Rec \uparrow	F1 \uparrow	Prec \uparrow	Rec \uparrow	F1 \uparrow		
BConformer-12	0.440	0.477	0.458	0.304	0.360	0.330	289.31	296.64
BConformer-9	0.428	0.463	0.445(-2.8%)	0.297	0.322	0.309(-6.4%)	219.94	225.50
BConformer-6	0.423	0.416	0.419(-8.5%)	0.249	0.296	0.270(-18.2%)	150.56	154.37
ResNet1D-152	0.442	0.484	0.462(+0.9%)	0.255	0.291	0.272(-17.6%)	196.41	201.45
ResNet1D-101	0.417	0.430	0.423(-7.6%)	0.242	0.238	0.240(-27.3%)	145.21	148.92
ViT1D-12	0.429	0.435	0.432(-5.7%)	0.269	0.334	0.298(-9.7%)	230.05	234.22
ViT1D-9	0.403	0.428	0.415(-9.4%)	0.276	0.311	0.292(-11.5%)	173.37	176.12

Table 3: Ablation studies evaluated on the validation set. BConformer-12 corresponds to BConformerR, and BConformer-9/6 reduces one layer of FCU-based CNN and Transformer for each stage compared to BConformer-12/9. ResNet bottlenecks adopt the same CNN blocks as Conformer, and ViT follows the design of Transformer branch.

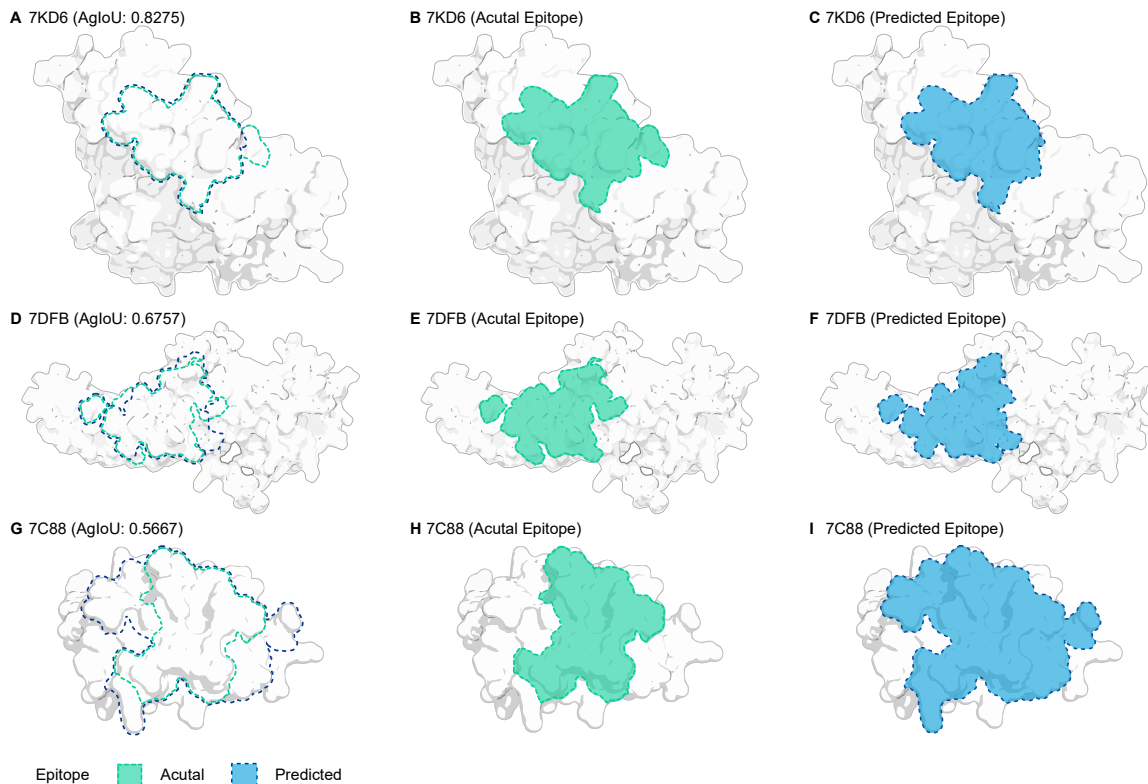


Figure 4: Structural visualization of epitopes predicted by BConformerR vs. actual epitopes. (A-C) Comparison of predicted and actual epitopes of 7KDB. Prediction is fully covered by the ground truth. (D-F) Comparison of predicted and actual epitopes of 7DFB. Prediction partially overlaps with the ground truth. (G-I) Comparison of predicted and actual epitopes of 7C88. Real epitopes are fully covered by the prediction.

Conformer mitigates this trade-off, as BConformer-9 outperforms ViT1D-12 on both linear and discontinuous F1 scores. Empirically, the hybrid design offers a more balanced solution for linear and discontinuous epitope prediction.

3.4 Case Studies

3.4.1 Predicted epitopes with high AgIoU

To visualize the prediction compared to the ground truth, we selected three antigen records from the test set with high AgIoU scores. Three overlap cases were shown in Figure 4: (1) the prediction is fully covered by the real epitopes (Fig. 4A-C), (2) the prediction partially overlaps with the real epitopes (Fig. 4D-F), (3) the real epitopes are entirely encompassed by the prediction (Fig. 4G-I).

4 Related Work

Numerous antibody-agnostic epitope prediction methods have been proposed. SEPPA-3.0 was the epitope prediction tool specifically designed for glycoproteins, based on the logistic regression classifier [15]. BepiPred-3.0 used embeddings from pretrained protein language models ESM-2 as input to a feedforward neural network (FFNN) to predict both linear and conformational B-cell epitopes [14]. Epitope3D modeled antigen surfaces as residue-level graphs and extracted distance-based graph signatures to train classifiers for conformational B-cell epitope prediction, with AdaBoost selected as the backbone [21, 35]. ScanNet was an end-to-end geometric deep learning model that learned interpretable residue-level features directly from 3D structural neighborhoods [20]. SEMA-1D 2.0 was constructed by adding a fully-connected linear layer on an ensemble of five ESM-2 models, while SEMA-3D 2.0 was developed upon an ensemble of five pre-trained SaProt models [11, 36]. DiscoTope-3.0 utilized inverse folding representations from ESM-IF1 and was trained on both predicted and solved structures using a positive-unlabelled ensemble strategy, enabling structure-based B-cell epitope prediction at scale [19, 37].

5 Conclusion

We present **BConformer**, a dual-branch Conformer model that integrates convolutional and self-attention mechanisms for residue-level prediction of both linear and conformational B-cell epitopes from antigen sequences. Two contributions are worth noting: (i) Adaptive *feature coupling and logit fusion* that balance information from the CNN and Transformer branches, yielding a well-calibrated score for each residue; (ii) a detailed *performance analysis on both linear and discontinuous epitopes*, which also validates the complementary effectiveness of both branches. Benchmark evaluation demonstrates that our model consistently outperforms strong sequence- and structure-based baselines, particularly on the more difficult task of predicting conformational epitopes. The anticipated beneficiaries include rational vaccine design, diagnostic reagent development and antibody engineering pipelines.

Acknowledgments

The computation resources in this study was sponsored by BayVax Biotech Limited. Y.-F. H. thanks support from the Major Program of the National Natural Science Foundation of China (92369201). The research was also supported by the National Key Research and Development Program of China (2021YFA0910700), the Health and Medical Research Fund, the Food and Health Bureau, The Government of the Hong Kong Special Administrative Region (COVID1903010, T-11-709/21-N) to J.-D.H. J.-D.H. also thanks the L & T Charitable Foundation, the Program for Guangdong Introducing Innovative and Entrepreneurial Teams (2019BT02Y198) and Shenzhen Key Laboratory for Cancer Metastasis and Personalized Therapy (ZDSYS20210623091811035) for their support.

References

- [1] Edgar Ernesto Gonzalez Kozlova, Loïc Cerf, Francisco Santos Schneider, Benjamin Thomas Viart, Christophe NGuyen, Bethina Trevisol Steiner, Sabrina de Almeida Lima, Franck Molina, Clara Guerra Duarte, Liza Felicori, et al. Computational b-cell epitope identification and production of neutralizing murine antibodies against atroxlysin-i. *Scientific reports*, 8(1):14904, 2018.
- [2] Rui Jia, Gaiping Zhang, Yilin Bai, Hongliang Liu, Yumei Chen, Peiyang Ding, Jingming Zhou, Hua Feng, Mingyang Li, Yuanyuan Tian, et al. Identification of linear b cell epitopes on cd2v protein of african swine fever virus by monoclonal antibodies. *Microbiology Spectrum*, 10(2):e01052-21, 2022.
- [3] Danniele L Vale, Amanda S Machado, Fernanda F Ramos, Daniela P Lage, Camila S Freitas, Daysiane de Oliveira, Nathalia C Galvani, Gabriel P Luiz, Mirian I Fagundes, Bruna B Fernandes, et al. Evaluation from a b-cell epitope-based chimeric protein for the serodiagnosis of tegumentary and visceral leishmaniasis. *Microbial Pathogenesis*, 167:105562, 2022.
- [4] Ivan Talucci and Hans M Maric. Epitope landscape in autoimmune neurological disease and beyond. *Trends in pharmacological sciences*, 45(9):768-780, 2024.
- [5] Alexandra R Dvorscek, Craig I McKenzie, Vera C Stäheli, Zhoujie Ding, Jacqueline White, Stewart A Fabb, Leonard Lim, Kristy O'Donnell, Catherine Pitt, Daniel Christ, et al. Conversion of vaccines from low to high immunogenicity by antibodies with epitope complementarity. *Immunity*, 57(10):2433-2452, 2024.
- [6] Esmaeil Roohparvar Basmenj, Susan Radman Pajhough, Afsane Ebrahimi Fallah, Elmira Rahimi, Hossein Atighy, Shadana Ghiabi, Shamim Ghiabi, et al. Computational epitope-based vaccine design with bioinformatics approach; a review. *Heliyon*, 11(1), 2025.
- [7] Gisela Brändén and Richard Neutze. Advances and challenges in time-resolved macromolecular crystallography. *Science*, 373(6558):eaba0954, 2021.
- [8] Pawel Rubach, Karolina A Majorek, Michal Gucwa, Krzysztof Murzyn, Alexander Wlodawer, and Wladek Minor. Advances in cryo-electron microscopy (cryoem) for structure-based drug discovery. *Expert Opinion on Drug Discovery*, (just-accepted), 2025.
- [9] Line Ledsgaard, Anne Ljungars, Charlotte Rimbault, Christoffer V Sørensen, Tulika Tulika, Jack Wade, Yessica Wouters, John McCafferty, and Andreas H Laustsen. Advances in antibody phage display technology. *Drug Discovery Today*, 27(8):2151-2169, 2022.
- [10] Tatiana I Shashkova, Dmitriy Umerenkov, Mikhail Salnikov, Pavel V Strashnov, Alina V Konstantinova, Ivan Lebed, Dmitriy N Shcherbinin, Marina N Asatryan, Olga L Kardymon, and Nikita V Ivanisenko. Sema: Antigen b-cell conformational epitope prediction using deep transfer learning. *Frontiers in immunology*, 13:960985, 2022.

- [11] Nikita V Ivanisenko, Tatiana I Shashkova, Andrey Shevtsov, Maria Sindeeva, Dmitriy Umerenkov, and Olga Kardymon. Sema 2.0: web-platform for b-cell conformational epitopes prediction using artificial intelligence. *Nucleic Acids Research*, 52(W1):W533–W539, 2024.
- [12] Jens Erik Pontoppidan Larsen, Ole Lund, and Morten Nielsen. Improved method for predicting linear b-cell epitopes. *Immunome research*, 2:1–7, 2006.
- [13] Martin Closter Jespersen, Bjoern Peters, Morten Nielsen, and Paolo Marcatili. Bepipred-2.0: improving sequence-based b-cell epitope prediction using conformational epitopes. *Nucleic acids research*, 45(W1):W24–W29, 2017.
- [14] Joakim Nøddeskov Clifford, Magnus Haraldson Høie, Sebastian Deleuran, Bjoern Peters, Morten Nielsen, and Paolo Marcatili. Bepipred-3.0: Improved b-cell epitope prediction using protein language models. *Protein Science*, 31(12):e4497, 2022.
- [15] Chen Zhou, Zikun Chen, Lu Zhang, Deyu Yan, Tiantian Mao, Kailin Tang, Tianyi Qiu, and Zhiwei Cao. Seppa 3.0—enhanced spatial epitope prediction enabling glycoprotein antigens. *Nucleic acids research*, 47(W1):W388–W394, 2019.
- [16] Zeming Lin, Halil Akin, Roshan Rao, Brian Hie, Zhongkai Zhu, Wenting Lu, Allan dos Santos Costa, Maryam Fazel-Zarandi, Tom Sercu, Sal Candido, et al. Language models of protein sequences at the scale of evolution enable accurate structure prediction. *BioRxiv*, 2022:500902, 2022.
- [17] Zeming Lin, Halil Akin, Roshan Rao, Brian Hie, Zhongkai Zhu, Wenting Lu, Nikita Smetanin, Robert Verkuil, Ori Kabeli, Yaniv Shmueli, et al. Evolutionary-scale prediction of atomic-level protein structure with a language model. *Science*, 379(6637):1123–1130, 2023.
- [18] Jens Vindahl Kringelum, Claus Lundegaard, Ole Lund, and Morten Nielsen. Reliable b cell epitope predictions: impacts of method development and improved benchmarking. *PLoS computational biology*, 8(12):e1002829, 2012.
- [19] Magnus Haraldson Høie, Frederik Steensgaard Gade, Julie Maria Johansen, Charlotte Würtzen, Ole Winther, Morten Nielsen, and Paolo Marcatili. Discotope-3.0: improved b-cell epitope prediction using inverse folding latent representations. *Frontiers in immunology*, 15:1322712, 2024.
- [20] Jérôme Tubiana, Dina Schneidman-Duhovny, and Haim J Wolfson. Scannet: an interpretable geometric deep learning model for structure-based protein binding site prediction. *Nature Methods*, 19(6):730–739, 2022.
- [21] Bruna Moreira da Silva, YooChan Myung, David B Ascher, and Douglas EV Pires. epitope3d: a machine learning method for conformational b-cell epitope prediction. *Briefings in Bioinformatics*, 23(1), 2022.
- [22] Johan Nilvebrant, Niklas Berndt Thalén, Johan Rockberg, and Magdalena Malm. An overview of epitopes and methods for antibody epitope mapping. *Epitope Mapping Protocols*, pages 1–11, 2025.
- [23] Anmol Gulati, James Qin, Chung-Cheng Chiu, Niki Parmar, Yu Zhang, Jiahui Yu, Wei Han, Shibo Wang, Zhengdong Zhang, Yonghui Wu, et al. Conformer: Convolution-augmented transformer for speech recognition. *arXiv preprint arXiv:2005.08100*, 2020.
- [24] Zhiliang Peng, Wei Huang, Shanzhi Gu, Lingxi Xie, Yaowei Wang, Jianbin Jiao, and Qixiang Ye. Conformer: Local features coupling global representations for visual recognition. In *Proceedings of the IEEE/CVF international conference on computer vision*, pages 367–376, 2021.
- [25] Jing Sun, Tianlei Xu, Shuning Wang, Guoqing Li, Di Wu, and Zhiwei Cao. Does difference exist between epitope and non-epitope residues? *Immunome research*, 7(3):1, 2011.
- [26] Saba Ferdous, Sebastian Kelm, Terry S Baker, Jiye Shi, and Andrew CR Martin. B-cell epitopes: Discontinuity and conformational analysis. *Molecular immunology*, 114:643–650, 2019.
- [27] Kaiming He, Xiangyu Zhang, Shaoqing Ren, and Jian Sun. Deep residual learning for image recognition. In *Proceedings of the IEEE conference on computer vision and pattern recognition*, pages 770–778, 2016.
- [28] Alexey Dosovitskiy, Lucas Beyer, Alexander Kolesnikov, Dirk Weissenborn, Xiaohua Zhai, Thomas Unterthiner, Mostafa Dehghani, Matthias Minderer, Georg Heigold, Sylvain Gelly, et al. An image is worth 16x16 words: Transformers for image recognition at scale. *arXiv preprint arXiv:2010.11929*, 2020.
- [29] Ashish Vaswani, Noam Shazeer, Niki Parmar, Jakob Uszkoreit, Llion Jones, Aidan N Gomez, Łukasz Kaiser, and Illia Polosukhin. Attention is all you need. *Advances in neural information processing systems*, 30, 2017.
- [30] Daniel Servén and Charlie Brummitt. pygam: Generalized additive models in python. *Zenodo*, 2018.
- [31] Yuwei Zhou, Wenwen Liu, Ziru Huang, Yushu Gou, Siqi Liu, Lixu Jiang, Yue Yang, and Jian Huang. A comprehensive antigen-antibody complex database unlocking insights into interaction interface. *eLife*, 14:RP104934, 2025.

- [32] Joakim Nøddeskov Clifford, Eve Richardson, Bjoern Peters, and Morten Nielsen. Abepitope-1.0: Improved antibody target prediction by use of alphafold and inverse folding. *Science Advances*, 11(24):eadu1823, 2025.
- [33] Milot Mirdita, Konstantin Schütze, Yoshitaka Moriwaki, Lim Heo, Sergey Ovchinnikov, and Martin Steinegger. Colabfold: making protein folding accessible to all. *Nature methods*, 19(6):679–682, 2022.
- [34] Matthew IJ Raybould, Aleksandr Kovaltsuk, Claire Marks, and Charlotte M Deane. Cov-abdab: the coronavirus antibody database. *Bioinformatics*, 37(5):734–735, 2021.
- [35] Cao Ying, Miao Qi-Guang, Liu Jia-Chen, and Gao Lin. Advance and prospects of adaboost algorithm. *Acta Automatica Sinica*, 39(6):745–758, 2013.
- [36] Jin Su, Chenchen Han, Yuyang Zhou, Junjie Shan, Xibin Zhou, and Fajie Yuan. Saprot: Protein language modeling with structure-aware vocabulary. *BioRxiv*, pages 2023–10, 2023.
- [37] Chloe Hsu, Robert Verkuil, Jason Liu, Zeming Lin, Brian Hie, Tom Sercu, Adam Lerer, and Alexander Rives. Learning inverse folding from millions of predicted structures. In *International conference on machine learning*, pages 8946–8970. PMLR, 2022.

Appendix

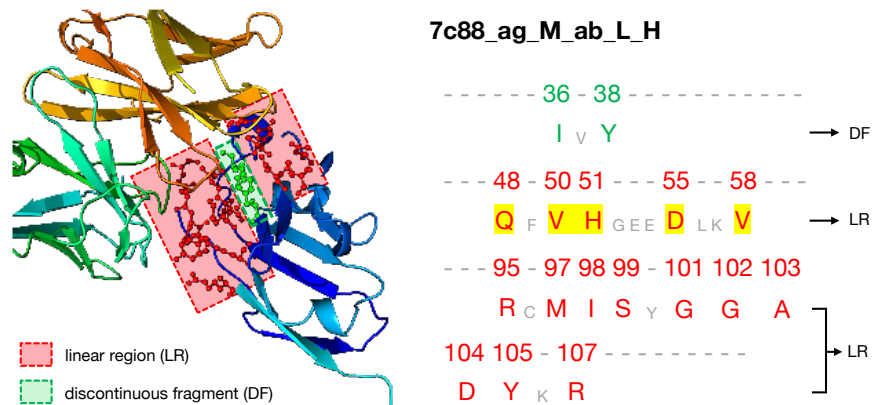


Figure 5: Linear regions and discontinuous fragments. (Left) The blue structure represents antigen 7c88, and the light green and light orange correspond to part of the antibody light chain and heavy chain, respectively; Linear regions are marked with red rectangles, and discontinuous fragments with green. (Right) Residues highlighted with numbers indicate epitopes.

A Linear Regions and Discontinuous Fragments

Regions are defined as linear stretches of antigen sequence having at least three antibody-contacting residues. Gaps between contacting residues are allowed, and a gap size of up to three non-contacting residues is chosen on the basis of the structure of α -helices, which enables residues on the same helical face to be included. Fragments, which do not contain enough antibody-contacting residues to qualify as a region (less than three), are considered discontinuous in our study (Fig. 5).

B Performance Metrics

The performance metrics used in this study include Precision (Prec), Recall (Rec), True Positive Rate (TPR), False Positive Rate (FPR), F1-score, Antigen-level intersection over union (AgIoU), Matthews correlation coefficient (MCC), whose definitions are given as follows:

$$\text{Prec} = \frac{\text{TP}}{\text{TP} + \text{FP}},$$

$$\text{Rec} = \frac{\text{TP}}{\text{TP} + \text{FN}},$$

$$\text{TPR} = \frac{\text{TP}}{\text{TP} + \text{FN}},$$

$$\text{FPR} = \frac{\text{FP}}{\text{FP} + \text{TN}},$$

$$\text{F1} = \frac{2\text{TP}}{2\text{TP} + \text{FP} + \text{FN}},$$

$$\text{AgIoU} = \frac{\text{TP}}{\text{TP} + \text{FP} + \text{FN}},$$

$$\text{MCC} = \frac{\text{TP} \cdot \text{TN} - \text{FP} \cdot \text{FN}}{\sqrt{(\text{TP} + \text{FP})(\text{TP} + \text{FN})(\text{TN} + \text{FP})(\text{TN} + \text{FN})}},$$

where TP, TN, FP and FN denote the number of true positives, true negatives, false positives and false negatives, respectively. The relationships between some of these metrics are given as:

$$F1 = \frac{2 \cdot \text{Prec} \cdot \text{Rec}}{\text{Prec} + \text{Rec}} = \frac{2 \cdot \text{AgIoU}}{1 + \text{AgIoU}},$$

$$\text{AgIoU} = \frac{2 \cdot F1}{2 - F1}.$$

C Ablation

C.1 ViT1D

Model	Embed Dim	Patch Size	Depth	Heads	MLP Ratio
ViT1D-9	1536	1	9	12	2.0
ViT1D-12	1536	1	12	12	2.0

Table 4: ViT variants used in ablation study.

We conducted ablation studies on two variants of the ViT1D model differing in depth: ViT1D-9 and ViT1D-12. As shown in Table 4, both models share the same embedding dimension (1536), input sequence length (1024), patch size (1), number of attention heads (12), and MLP expansion ratio (2.0). The only difference is the number of transformer encoder layers.

C.2 ResNet1D

Stage	Output Channels	Kernel Size	ResNet1D-101	ResNet1D-152
input	1152	-	✓	✓
stem	288	7	✓	✓
layer1	576 (144 × 4)	3	3	3
layer2	1152 (288 × 4)	3	4	8
layer3	2304 (576 × 4)	3	23	36
layer4	4608 (1152 × 4)	3	3	3
classifier	2	1	✓	✓

Table 5: ResNet architectures used in ablation study.

We employed two variants of the ResNet1D backbone in the ablation studies: ResNet1D-101 and ResNet1D-152. As shown in Table 5, both models accept input feature maps with 1152 channels and begin with an initial convolutional layer producing 320 channels. The networks consist of four residual stages of bottlenecks with the expansion factor of 4, each stage starting by downsampling the channel dimension to half. The difference lies in the number of bottleneck blocks per stage. ResNet1D-101 contains [3, 4, 23, 3] blocks across the four layers, while ResNet1D-152 is deeper with [3, 8, 36, 3] blocks. The final output is projected to the target classes through a 1×1 convolutional layer. .